Pseudocapacitance boosted N-doped carbon coated Fe$_7$S$_8$ nano-aggregates as promising anode materials for lithium and sodium storage

Yanli Zhou[1], Ming Zhang[1], Qi Wang[1], Jian Yang[2], Xingyun Luo[3], Yanlu Li[3], Rong Du[1], Xinsheng Yan[1], Xueqin Sun[1], Caifu Dong[1], Xiaoyu Zhang[1], and Fuyi Jiang[1] (✉)

[1] School of Environmental and Material Engineering, Yantai University, Yantai 264005, China
[2] Key Laboratory of Colloid and Interface Chemistry, Ministry of Education School of Chemistry and Chemical Engineering, Shandong University, Jinan 250100, China
[3] Institute of Crystal Materials and State Key Laboratory of Crystal Materials, Shandong University, Jinan 250100, China

ABSTRACT

Herein, the core–shell structured N-doped carbon coated Fe$_7$S$_8$ nano-aggregates (Fe$_7$S$_8$@NC) were controllably prepared via a simple three-step synthesis strategy. The appropriate thickness of N-doped carbon layer outside Fe$_7$S$_8$ nano-aggregates can not only inhibit the particle pulverization induced by the big volume changes of Fe$_7$S$_8$, but can increase the electron transfer efficiency. The hierarchical Fe$_7$S$_8$ nano-aggregates composed of some primary nanoparticles can accelerate the lithium or sodium diffusion kinetics. As anode materials for Li-ion batteries (LIBs), the well-designed Fe$_7$S$_8$@NC nanocomposites exhibit outstanding lithium storage performance, which is better than that of pure Fe$_7$S$_8$, Fe$_3$O$_4$@NC and Fe$_7$S$_8$@C. Among these nanocomposites, the N-doped carbon coated Fe$_7$S$_8$ with carbon content of 26.87 wt.% shows a high reversible specific capacity of 833 mAh·g^{-1} after 1,000 cycles at a high current density of 2 A·g^{-1}. The above electrode also shows excellent high rate sodium storage performance. The experimental and theoretical analyses indicate that the outstanding electrochemical performance could be attributed to the synergistic effect of hierarchical Fe$_7$S$_8$ nanostructure and conductive N-doped carbon layer. The quantitative kinetic analysis indicates that the charge storage of Fe$_7$S$_8$@NC electrode is a combination of diffusion-controlled battery behavior and surface-induced capacitance behavior.

KEYWORDS

Fe$_7$S$_8$, N-doped carbon, anode materials, Li-ion batteries, Na-ion batteries

1 Introduction

As one of the most popular energy storage systems, Li-ion batteries (LIBs) have been widely applied in portable electronic devices and electric vehicles due to their high energy densities and power densities [1, 2]. However, the high price and scarcity of lithium resources limit their further development in the large-scale energy devices. Na-ion batteries (SIBs) as one of the potential alternatives to LIBs have attracted great attentions due to the low cost of sodium and abundant natural reserves compared to LIBs [3]. Anode materials are the key factors which can affect the electrochemical performance of LIBs and SIBs. The similar reaction processes of Na to Li make it feasible that the anode materials of LIBs can also be applied in SIBs. Nonetheless, the commercial graphite for LIBs cannot satisfy the increasing energy requirement because of its low specific capacity (372 mAh·g^{-1}) and safety problems induced by the low voltage platform [4]. Besides, graphite is unsuitable to accommodate larger Na$^+$, and no commercially available anode material was currently developed. So, it is essential to develop new high-performance anode materials for both LIBs and SIBs.

Recently, metal sulfides have been considered as the advanced anode materials in virtue of high theoretical specific capacity, good conductivity and small electrode polarization [5–9]. Among these anode materials, iron sulfides such as Fe$_7$S$_8$ and FeS have been paid much attentions for its high capacity, eco-friendliness, earth abundancy and low-cost features [10–12]. However, the big volume changes induced by the conversion reaction during cycling will result in the material pulverization and rapid capacity decay. The dissolution of polysulfide (Li$_2$S$_n$, $4 \leq n \leq 8$) into the organic electrolyte is another key problem. Many efforts have been devoted to searching for effective strategies to improve the electrochemical performance of iron sulfides. One method is to design unique nanostructure especially the hierarchical architectures to short the electron/ion diffusion paths and buffer the volume expansion upon cycling [13, 14]. Another way is to hybrid with some carbonaceous materials to improve the conductivity, suppress the volume changes and prevent the dissolution of polysulfides [15–20]. For example, the composite of FeS nanoparticles and carbon nanosheets exhibited excellent lithium storage performance, its reversible capacity could maintain at 703 mAh·g^{-1} over 150 cycles at 1 A·g^{-1} [16]. N-doping can create more defects, which can offer more

---

active sites, benefiting for the Li^+ or Na^+ storage [21, 22]. Thus, N-doped carbon coating is usually regarded as an effective way to improve the electrochemical performance of active materials [23–28]. For instance, the hybrid of MnO and N-doped carbon showed better lithium storage performance than carbon-modified MnO [26]. The yolk–shell structured pyrrhotite@N-doped carbon electrodes for SIBs exhibited a high reversible capacity of 594 mAh·g^{-1} after 100 cycles at 100 mA·g^{-1}. However, the big particle size of pyrrhotite will influence the sodium diffusion dynamics and induce the incomplete redox reactions, which will result in the low specific capacity [27]. Based on the previous reports, the combination of hierarchical nanostructures and N-doped carbon materials can improve the lithium and sodium storage performance of electrode materials. However, how to design N-doped carbon modified iron sulfide hybrids with fast ion and electron transport to obtain excellent electrochemical performance is still a challenge for researchers.

In this paper, the N-doped carbon coated hierarchical Fe_7S_8 nano-aggregates (Fe_7S_8@NC) have been successfully prepared by a three-step synthesis strategy. Different Fe_7S_8@NC nano-composites can be obtained by changing the amount of dopamine hydrochloride and annealing temperature. The introduction of nitrogen atom in the carbon layer creates more defects, which can offer more active sites for lithium or sodium storage, and increase the electronic conductivity. The Fe_7S_8 nano-aggregates can promote the lithium or sodium diffusion kinetics. The outer N-doped carbon layer can accommodate the volume change of the inner Fe_7S_8 active materials and enhance the electron transfer efficiency. As expected, the optimized Fe_7S_8@NC electrodes demonstrate outstanding electrochemical performances for both LIBs and SIBs.

2 Experimental section

2.1 Synthesis of Fe_7S_8@NC nanocomposites

The Fe_3O_4 nano-aggregates and dopamine coated Fe_3O_4 (Fe_3O_4@PDA) nanocomposites were prepared via a previously reported method [23]. Briefly, the Fe_3O_4 nano-aggregates were obtained by separately adding 2 mmol $FeCl_3$ and 0.9 g polyacrylic acid (PAA) into 20 mL ethylene glycol and stirred for several minutes to obtain a uniform solution. Then, 5 mL ammonia monohydrate (NH_3·H_2O, 25%–28%) was added and stirred until the color of solution changes from orange to amaranth. The final solution was transferred to a Teflon-lined stainless-steel autoclave and kept at 230 °C for 2 h in the oven. After that it was cooled to room temperature, the precipitate was collected, washed with deionized water and alcohol thoroughly and dried to obtain Fe_3O_4 black powder. The Fe_3O_4@PDA composites were prepared by adding dopamine hydrochloride into 0.1 g Fe_3O_4 dispersed 50 mL Tris-buffer solution. The mixture was stirred for 5 h at room temperature. Then the dispersion was centrifuged and washed with deionized water and alcohol thoroughly and dried to obtain the black product. For the synthesis of Fe_7S_8@NC nanocomposites, the above prepared Fe_3O_4@PDA nanocomposites using dopamine hydrochloride of 0.08 g and sulfur powder with a weight ratio of 1:4 were mixed by grinding in the mortar, the mixture were placed in the porcelain boat, and transferred into a tube furnace for sulfurization under Ar atmosphere. The mixture was first sintered at 150 °C for 2 h, then raised to 550 °C with a rate of 5 °C·min^{-1} and kept at 550 °C for 3 h. The final products using dopamine hydrochloride of 0.05, 0.08 or 0.12 g were abbreviated to Fe_7S_8@NC-1, Fe_7S_8@NC-2 and Fe_7S_8@NC-3, respectively. The obtained products calcined at 450, 550 and 650 °C were abbreviated to Fe_7S_8@NC-450, Fe_7S_8@NC-550 and Fe_7S_8@NC-650, respectively. The Fe_3O_4@NC and pure Fe_7S_8 nanoparticles were also prepared using a similar method. The Fe_7S_8@C was also prepared using glucose as carbon sources as comparison.

2.2 Sample characterization

The structures of obtained products were characterized by X-ray diffractometer (Shimadzu XRD-7000, Japan) and Raman spectroscopy (HORIBA LabRAM HR Evolution, France) with 532 nm laser excitation. The morphologies were observed by transmission electron microscopy (TEM, JEOL-1400Plus, Japan), high-resolution TEM (HRTEM, JEM-2100F, 200 kV) and field emission scanning electron microscopy (FESEM, JSM-7610F, Japan) equipped with an energy-dispersive spectroscopy (EDS). X-ray photoelectron spectroscopy (XPS) was obtained on an ESCALAB 250 spectrometer (ThermoFisher Sci., USA). Thermogravimetric (TG, Netzsch Sta 449F3, Germany) analysis was measured from room temperature to 800 °C at a heating rate of 10 °C·min^{-1} in O_2 atmosphere. Nitrogen sorption isotherm was performed at 77.3 K on a Micromeritics ASAP2020HD88 gas sorptometer (Micromeritics, USA).

2.3 Electrochemical measurements

The working electrode was prepared by grinding active material (Fe_3O_4@NC, Fe_7S_8 or Fe_7S_8@NC), acetylene black, and carboxyl methyl cellulose (CMC) mixture (with a weight ratio of 7:2:1) with water as dispersant. Then, the above slurry was coated onto a copper foil, and dried at 60 °C in vacuum for 10 h. The average mass loading of electrodes was about 1.0–1.5 mg·cm^{-2}. The CR2032-type coin half cells for LIBs were assembled in an argon-filled glovebox, using lithium foil as counter electrode, Celgard 2400 microporous polypropylene membrane as separator, and electrolyte is a solution of 1 M $LiPF_6$ in ethylene carbonate (EC) and dimethyl carbonate (DMC) (1:1 v/v). For SIBs assembly, the pure sodium foil was used as counter electrode, the electrolyte was 1 M $NaClO_4$ in EC/propylene carbonate (PC) (1:1 v/v), containing 5 wt.% fluoroethylene carbonate (FEC) as an additive. Glass fiber (GF/D) from Whatman was used as a separator. The full cells were assembled with Fe_7S_8@NC as anode and $LiCoO_2$ or $Na_3V_2(PO_4)_3$ as cathode. The capacity ratio between cathode and anode was controlled at 1:1.2. The capacities for the full cells were calculated by the mass of Fe_7S_8@NC. Galvanostatic charge–discharge curves, cycling performances and rate capabilities were tested on a battery testing system (Land CT2001A, China). All the specific capacities were calculated on the basis of total mass of the composites. Cyclic voltammetry (CV) curves were obtained from an electrochemical workstation (LK2005A, China). Electrochemical impedance spectra (EIS) were measured on an electrochemical workstation (AUTOLAB PGSTAT302N, Switzerland) over a frequency range of 100 kHz to 0.01 Hz with an amplitude of 10 mV. All the electrochemical tests were carried out at 25 °C.

2.4 Computational details

The calculations were carried out in the Vienna *ab initio* simulation package (VASP) implementation of density functional theory (DFT) in conjunction with the projector-augmented-wave (PAW) formalism. The Perdew–Burke–Ernzerhof (PBE) functional within generalized gradient approximation (GGA) form was adopted to describe the electron exchange-correction interactions. Thereby the C $2s^22p^2$, N $2s^22p^3$, S $3s^23p^4$ and Fe $3d^64s^2$ states were treated as valence electrons. The plane-wave basis set was restricted by a kinetic energy cutoff of 400 eV. The Fe_7S_8 cluster was optimized by putting it in a cubic unit

cell of 20 Å × 20 Å × 20 Å. The carbon layer model was constructed by using an 8 × 8 graphene supercell with 128 atoms. A vacuum space of 18 Å was added along *z* direction in order to eliminate the interaction between the atoms layers and avoid the interference of periodic arrangement. The graphitic N model was constructed by substituting one C atom by one N atom. The pyridinic N model was obtained by removing one C atom to form a vacancy and then substituting one adjacent C atom which belongs to the six-membered carbon ring by one N atom. The pyrrolic N model was constructed by placing the N atom at the space of the four C atoms near the C vacancy based on the pyridinic N structure. For structural optimizations, the convergent criterion of total energy and the force acting on every atom were set as 10^{-3} eV and 0.05 eV·Å^{-1}, respectively. The Monkhorst-Pack scheme was adopted for sampling the Brillouin zone with a k-mesh of 4×4×1 for all systems.

The binding ability of Fe_7S_8 cluster with carbon layer, graphitic N, pyridinic N and pyrrolic N models is evaluated by the adsorption energy (E_{ads}) that is defined as

$$E_{ads} = E_{tot} - E_{layer} - E_{Fe7S8} \tag{1}$$

where E_{tot}, E_{layer}, and E_{Fe7S8} are the total energies of the Fe_7S_8-adsorbed layer structure, the isolated layer structure, and the isolated Fe_7S_8 cluster, respectively. Hence, by definition, the negative value of E_{ads} corresponds to the favorable adsorption of Fe_7S_8 cluster on the layer structure.

3 Results and discussion

Scheme 1 shows the synthesis process of Fe_7S_8@NC nano-composites. First, the Fe_3O_4 nano-aggregates were fabricated via a facile solvothermal method [23]. Second, the dopamine as carbon resources was successfully coated on the surface of Fe_3O_4 nano-aggregates via a simple polymerization reaction, and three Fe_3O_4@PDA nanocomposites were obtained by adjusting the addition contents of dopamine hydrochloride. Third, the Fe_3O_4@PDA and sulfur powder were evenly mixed together, and then the mixture was annealed at 150 °C for 2 h to ensure sulfur stream diffuse into the surface of Fe_3O_4. After that it was further held at a constant high temperature for 3 h. During this process, the PDA will decompose to N-doped carbon, and the sulfur vapor will react with Fe_3O_4@PDA, leading to the phase transformation of Fe_3O_4 to Fe_7S_8. Finally, the Fe_7S_8@NC nanocomposites were obtained.

Figure 1(a) shows the X-ray diffraction (XRD) pattern of typical Fe_7S_8@NC nanocomposite (Fe_7S_8@NC-2), four strong diffraction peaks at 30.0°, 34.0°, 44.0° and 53.3° are assigned as (200), (203), (206) and (220) crystal planes of pyrrhotite-3T Fe_7S_8 (JCPDS No. 24-0220). Besides the Fe_7S_8 diffraction peaks, no other obvious impurity peaks are observed. The corresponding carbon peak is not distinct due to its amorphous features. The Raman spectrum was used to verify the existence of carbon. As shown in Fig. 1(b), two characteristic peaks of carbon located at around 1,356 and 1,545 cm^{-1} are attributed to the D and G bands for carbon materials, respectively [28–30]. Another weak peak located at 213 cm^{-1} confirms the presence of Fe_7S_8 [16, 31]. EDS spectrum in Fig. S1 in the Electronic Supplementary Material (ESM) also shows the existence of five elements containing C, N, O, Fe and S, and the atomic ratio of Fe to S is calculated as 1:1.26, suggesting the formation of Fe_7S_8, which is in accordance with that of XRD pattern. XPS was carried out to further confirm the valance states and element composition of Fe_7S_8@NC nanocomposite. Figures 1(c)–1(f) show the high-resolution XPS spectra of C1s, N1s, Fe2p and

S2p. For C1s spectrum, three peaks located at 284.8, 285.8 and 287.2 eV are attributed to the C–C, C–N and C=O groups, respectively [10, 13]. Three peaks at 398.4, 399.8 and 400.8 eV for N1s correspond to pyridinic, pyrrolic and graphitic N species [32]. The introduction of N atom in the carbon layer can provide more active sites for lithium or sodium storage [11]. For Fe2p spectrum, two main peaks located at 710.5 and 723.9 eV are ascribed to Fe^{2+}, and the other two main peaks at 713.4 and 726.7 eV imply the presence of Fe^{3+} species [10, 33]. A couple of peaks located at 719.4 and 732.1 eV can be attributed to the satellite peaks. The small peak at 706.9 eV indicates the generation of metallic Fe during the annealing process. In the S2p spectrum, five peaks can be obtained, the three peaks at 161.4, 162.6 and 163.7 eV are assigned as S^{2-}, S_2^{2-} and S_n^{2-}, respectively, another peak centered at 164.6 eV belongs to S, and a wide peak at 168 eV is attributed to SO_4^{2-}, resulting from the oxidation of S^{2-} in air [34]. All the above results suggest the successful preparation of Fe_7S_8@NC nano-composites. Moreover, the as-obtained Fe_7S_8@NC nano-composites with dopamine hydrochloride of 0.05 and 0.12 g as well as Fe_7S_8@C show similar XRD patterns with Fe_7S_8@NC-2 (Fig. S2 in the ESM). Nevertheless, the annealing temperature is considered as an important factor to affect the phase and structure. When the annealing temperature is 450 °C, a mixture of Fe_7S_8 and FeS_2 with poor crystallinity is obtained. While when the temperature is increased to 650 °C, the product is still hexagonal phase Fe_7S_8, the stronger diffraction peaks implies the increase of crystallinity (Fig. S3 in the ESM).
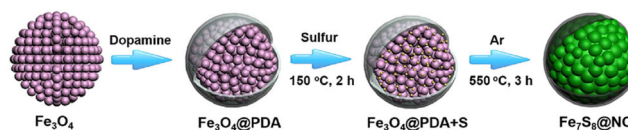
Scheme 1 Synthesis process of Fe_7S_8@NC nanocomposites.

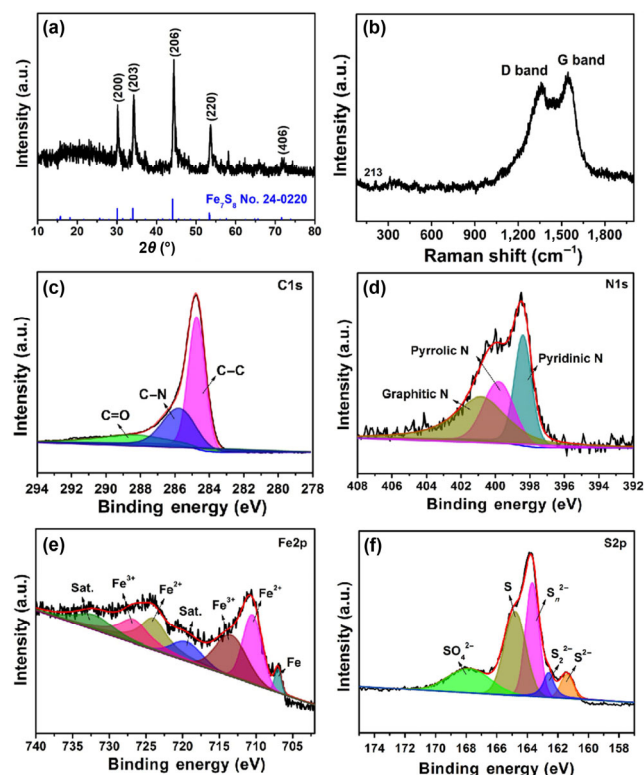**Figure 1** (a) XRD pattern, (b) Raman spectrum, and high-resolution XPS spectra of (c) C1s, (d) N1s, (e) Fe2p and (f) S2p of Fe_7S_8@NC nanocomposite.

The morphology and microstructure of the typical Fe₇S₈@NC nanocomposite were investigated by SEM and TEM techniques (Fig. 2). The SEM image in Fig. 2(a) shows that Fe₇S₈@NC nanocomposite is well dispersed nanospheres. The magnified SEM image shows that it presents a smooth surface after carbon coating (Fig. 2(b)). And the average particle size is about 50 nm. Low-magnification TEM image in Fig. 2(c) further shows that the well-dispersed Fe₇S₈@NC nanocomposite has a core–shell nanostructure, and the particle size is in agreement with that of SEM image. Figure 2(d) exhibits the magnified TEM image of typical Fe₇S₈@NC nanocomposite. The core–shell nanostructure can be clearly observed, and the Fe₇S₈ core is consisted of several small nanoparticles with an average particle size of 10–20 nm (Fig. 2(e)), implying that the morphology of nano-aggregates can be maintained after sulfuration. Besides, the average thickness of outer carbon layer is about 8 nm. When the amount of dopamine hydrochloride is 0.05 or 0.12 g, the related thickness of carbon layer is about 5 or 12 nm (Fig. S4 in the ESM). Owing to the phase changes from Fe₃O₄ to Fe₇S₈, the primary particle size of Fe₇S₈ distinctly increases in comparison with that of Fe₃O₄. Reaction temperature plays an important role in the morphology and particle size of products. As the reaction temperature rises from 450 to 650 °C, the overall particle size of inner active materials obviously increases, and the cluster-like morphology of Fe₇S₈ core for Fe₇S₈@NC-650 can hardly be found (Fig. S5 in the ESM) due to rapid high temperature reaction. Anyway, the core–shell structure is well maintained due to the protection effect of outer carbon layer. Without the carbon layer, the irregular Fe₇S₈ particles are obtained (Fig. S4(b) in the ESM). Figure 2(f) exhibits the related HRTEM image. The obvious lattice fringes with an interplanar spacing of 0.595 and 0.263 nm are corresponding to the (200) and (203) planes of pyrrhotite-3T Fe₇S₈. The outer disordered carbon layer implies its amorphous features [35]. The corresponding selected area electron diffraction (SAED) pattern is shown in Fig. 2(g). Four obvious diffraction rings from inner to outside are attributed to (200), (203), (206) and (220) crystal planes of pyrrhotite Fe₇S₈. Moreover, the

elemental mapping (Fig. 2(h)) indicates the coexistence of Fe, S, C and N elements. It further confirms that the inner core is Fe₇S₈, and outer shell is N-doped carbon. Besides, according to the TG curves, the weight percent of carbon layer for different nanocomposites (Fe₇S₈@NC-1, Fe₇S₈@NC-2 and Fe₇S₈@NC-3) is estimated to be 22.33 wt.%, 26.87 wt.% and 33.88 wt.%, respectively (Fig. S7 in the ESM).

The N_2 adsorption–desorption isotherm of typical Fe₇S₈@NC nanocomposite shows a distinct hysteretic loop for P/P_0 ranges from 0.8 to 1.0 (Fig. S8(a) in the ESM), implying the existence of some mesopores in the nanocomposite. The pore size is mainly located at about 27 and 34 nm (Fig. S8(b) in the ESM), which is originated from the voids between Fe₇S₈@NC. A small amount of micropores located at 1.3 nm are possibly attributed to the voids between Fe₇S₈ primary nanoparticles. The specific surface area (48.15 $m^2 \cdot g^{-1}$) and porous structure benefit the penetration of electrolyte and facilitate the transport of electrons and lithium or sodium ions [36, 37], which could improve the electrochemical performance of Fe₇S₈@NC nanocomposite.

The well-designed core–shell structured Fe₇S₈@NC nanocomposites inspire us to investigate their lithium and sodium performances. The electrochemical performance of Fe₇S₈@NC nanocomposites for LIBs are shown in Fig. 3. Figure 3(a) shows the CV curves of typical Fe₇S₈@NC nanocomposite for the first three cycles with a scan rate of 0.1 $mV \cdot s^{-1}$. In the first cathodic scan, one wide peak at 1.6 V is resulted from the lithium intercalation into Fe₇S₈ to form Li_2FeS_2 [10, 13]. The strong peak at 1.09 V is attributed to the reduction of Li_2FeS_2 to Fe and Li_2S. The weak peak around 0.7 V corresponds to the formation of solid electrolyte interphase (SEI) film on the surface of active material. In the subsequent two cycles, the main reduction peak shifts from 1.09 to 1.4 V owing to the irreversible structure changes, which is related to the formation of $Li_{2-x}FeS_2$. In the first anodic scan, a strong peak at 1.93 V and a weak peak at about 2.36 V are observed, which is ascribed to the oxidation of Fe to form Li_2FeS_2, and Li_2FeS_2 to form Fe_3S_4, respectively. However, the weak peak located at 2.36 V disappears gradually as the cycle numbers increase, which is
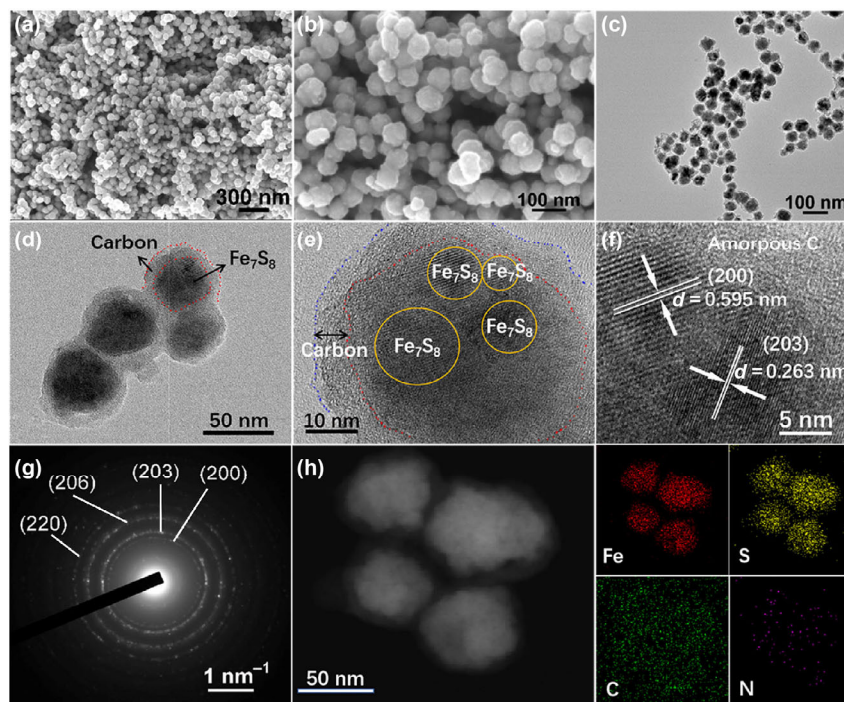

Figure 2 (a) and (b) SEM images, (c) and (d) TEM images, (e) and (f) HRTEM images, (g) SAED pattern, and (h) EDS elemental mapping of Fe₇S₈@NC nanocomposite.

possibly resulted from the irreversible electrochemical reaction [13]. The structure evolution process has been confirmed by *ex-situ* XRD and HRTEM techniques (Figs. S9 and S10 in the ESM). The overlap of second and third CV curves indicates good reversibility of the redox reactions of Fe_7S_8@NC nanocomposites. Figure 3(b) shows the galvanostatic discharge/charge profiles for the first, second and fifth cycles at a current density of 0.1 A·g^{-1}. The initial discharge and charge capacity are 1,553 and 1,029 mAh·g^{-1}, respectively, with an initial Coulombic efficiency (CE) of 66.3%. The first large irreversible capacity is usually resulted from the formation of SEI film. Two voltage plateaus located at 1.3 and 0.8 V can be clearly observed for the initial discharge process. For the second and fifth cycles, the voltage plateau rises to 1.4 V. The voltage plateau for all the charge curves are located at 1.9 V, and no obvious changes are found. This result is in agreement with that of CV curves. The other nanocomposites also exhibit similar CV curves and discharge/charge profiles (Figs. S11 and S12 in the ESM). Figure 3(c) shows the cycling performance of Fe_3O_4@NC and Fe_7S_8@NC nanocomposites. The Fe_7S_8@NC nanocomposites show good cycling stability without distinct capacity decay. The charge specific capacity can retain at 944 mAh·g^{-1} after 100 cycles. While the specific capacity for the Fe_3O_4@NC nanocomposites is only maintained at 688 mAh·g^{-1}. The possible reasons for performance difference are as follows: (1) The Fe_7S_8 has smaller electrode polarization, which will lead to the better rate performance. (2) The high conductivity of Fe_7S_8 will benefit the electron transfer. (3) The small charge transfer impedance and rapid ion diffusion behavior of Fe_7S_8 will enhance the lithium transport kinetics.

The effect of carbon contents on the electrochemical performance of Fe_7S_8@NC nanocomposites for LIBs was discussed. Figure 3(d) shows the rate capability of different Fe_7S_8@NC nanocomposites. The average reversible capacity of Fe_7S_8@NC-2 from 0.1 to 5 A·g^{-1} is 997, 913, 845, 80, 761 and 677 mAh·g^{-1}, respectively. When the current density goes back to 0.1 A·g^{-1}, the average capacity is as high as 1,016 mAh·g^{-1}, demonstrating good reversibility, which is better than the other nanocomposites including Fe_3O_4@NC nanocomposites (Fig. S13 in the ESM). As shown in Fig. 3(e), the Fe_7S_8@NC-2 nanocomposite shows the highest specific capacity and best cycling stability during all the nanocomposites when cycled at

2 A·g^{-1}. The reversible capacity can maintain at 833 mAh·g^{-1} after 1,000 cycles, this result is obviously better than that of Fe_7S_8@C (Fig. S14 in the ESM). This electrochemical result is superior to the previous references (Table S1 in the ESM). The excellent cycling performance and rate capability of Fe_7S_8@NC nanocomposites are mainly attributed to the high conductivity and good crystal structure of Fe_7S_8. Besides, the Fe^0 can take part in the charge reactions, which contributes to additional specific capacity [38]. As the carbon layer thickness increases, the cycling stability of Fe_7S_8@NC nanocomposites enhances, however, the specific capacity will decrease due to the increase of carbon contents. According to the results, appropriate carbon contents are essential to enhance the lithium storage performance of Fe_7S_8@NC nanocomposites. Besides, the core–shell structures of Fe_7S_8@NC-2 and Fe_7S_8@NC-3 nanocomposites can be well retained after 1,000 cycles at 2 A·g^{-1}, which is in accordance with the above obtained excellent electrochemical performance as (Figs. S15 and S16 in the ESM). Furthermore, the effect of annealing temperature on the lithium storage performance of Fe_7S_8@NC nanocomposites was also investigated. As shown in Fig. S17 in the ESM, combined with the results of cycling performance and rate capability, the Fe_7S_8@NC-550 still presents the best lithium storage performance during all the nanocomposites. The lower specific capacity for Fe_7S_8@NC-650 is ascribed to the bigger particle size of sphere-like Fe_7S_8, which limits the lithium diffusion behavior and makes the redox reaction incomplete.

The EIS results further demonstrate the electrochemical behavior of obtained Fe_7S_8@NC nanocomposites for LIBs. As shown in Fig. 4(a) and Fig. S18(a) in the ESM, all the Nyquist plots for the cycled electrodes show two depressed semicircles in the high frequency region and a straight line in the low frequency region. The two depressed semicircles are attributed to the SEI film and the charge transfer impedances (R_f and R_{ct}) [39]. It can be observed that the R_f and R_{ct} values of Fe_7S_8@NC nanocomposites are obviously smaller than those of Fe_3O_4@NC composites, which is attributed to the so-called electrochemical milling effect [40]. The Fe_7S_8@NC-2 nanocomposite shows the smallest R_f and R_{ct} values in contrast with those of the other nanocomposites, benefiting the diffusion kinetics upon cycling (Table S2 in the ESM). Besides, the diffusion coefficients of lithium ion (D_{Li^+}) of different samples were also evaluated
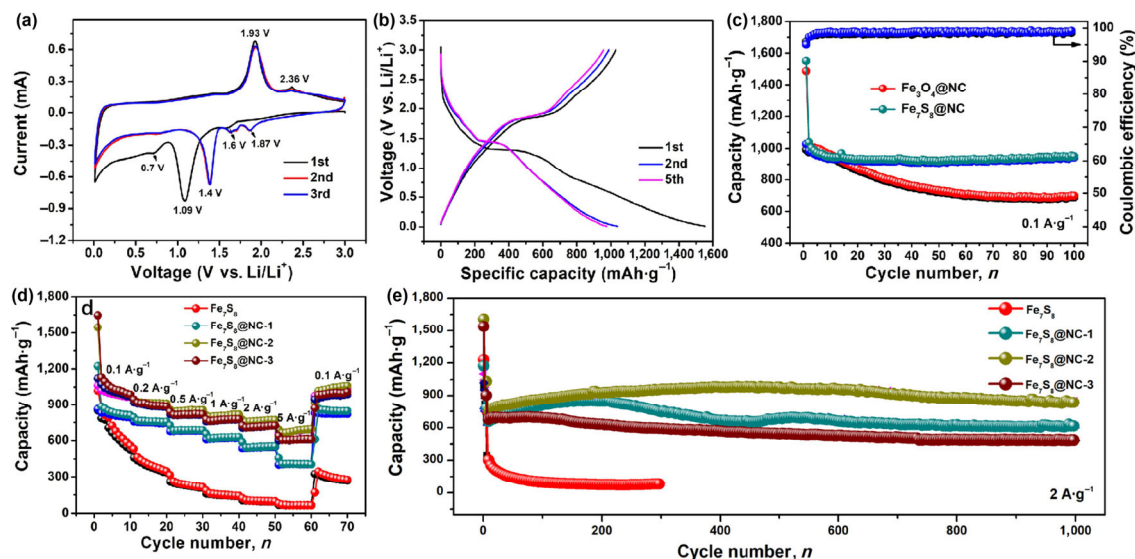

Figure 3 (a) CV curves for the first three cycles and (b) discharge/charge profiles for the first, second and fifth cycles of Fe_7S_8@NC nanocomposite at 0.1 A·g^{-1}. (c) Cycling performance and Coulombic efficiency at 0.1 A·g^{-1}, (d) rate capability at different current densities and (e) cycling performance at 2 A·g^{-1} of Fe_7S_8 and Fe_7S_8@NC nanocomposites.

based on the following equation [41]

$$D_{Li^+} = R^2T^2/2S^2n^4F^4C^2\sigma^2 \qquad (1)$$

where the R and T correspond to the gas constant and absolute temperature, respectively; S and n represent the surface area of electrode and the number of electrons per molecule involved in the redox process; F is the Faraday constant; C is the molar concentration of Li^+ and σ is the Warburg factor. σ can be obtained by plotting Z' versus $\omega^{-1/2}$ from its slope according to Eq. (2) [42]

$$Z' = R_D + R_L + \sigma\omega^{-1/2} \qquad (2)$$

According to the above equations, a small slope value implies a small Warburg factor, corresponding to a large Li^+ ion diffusion coefficient. Figure 4(b) and Fig. S18(b) in the ESM show the fitted straight lines of Z' versus $\omega^{-1/2}$ at low frequency of different samples. It can be seen that the slope of Fe_7S_8@NC-2 is obviously lower than that of Fe_3O_4@NC, demonstrating the rapid ion diffusion process. The three Fe_7S_8@NC nanocomposites show lower slope value than pure Fe_7S_8 due to the introduction of N-doped carbon layer, as the carbon contents increase, the slope gradually decreases, implying enhanced Li^+ transport kinetics.

Galvanostatic intermittent titration technique (GITT) was also employed to study the lithium reaction kinetics (Fig. S20 in the ESM) [43, 44]. It can be observed that the Fe_7S_8@NC anode exhibits smaller overpotential than pure Fe_7S_8 anode, and the calculated D values are also an order of magnitude bigger than that of the pure Fe_7S_8 anode. The increased D values confirm the rapid lithium diffusion ability by introducing the N-doped carbon layer. The kinetics process and the charge storage mechanism of Fe_7S_8@NC-2 electrode were further analyzed by the CV curves at different scan rates ranging from 0.2 to 1.0 mV·s⁻¹. As shown in Fig. 4(c), both the cathodic and anodic currents increase with the increase of scan rate. Generally, the peak current (i_p) presented in the CV curves during cathodic/anodic scans and scan rate (v) obeyed the relationships as following [45]

$$i_P = av^b \qquad (3)$$

The b value can be determined by the of log i_p vs. log v plot.

When the b value is close to 0.5, it refers to a diffusion-controlled electrochemical process, while a value of 1.0 represents a surface capacitive electrochemical process [46, 47]. After calculation, the b-values of peak 1, peak 2 and peak 3 are 0.74, 0.64, 0.81, respectively (Fig. 4(d)), showing a mixture of lithium storage mechanisms containing both diffusion-controlled and surface capacitive related electrochemical process. Furthermore, the contributions of diffusion-controlled and surface capacitive can be separated at a certain scan rate based on the following equation

$$i(v) = k_1v + k_2v^{1/2} \qquad (4)$$

where $i(v)$ corresponds to current density at a fixed potential, and k_1 and k_2 are constants at the given potential. Particularly, k_1v and $k_2v^{1/2}$ stand for the diffusion-controlled and surface capacitive contribution, respectively. The capacitive contributions are calculated to be 83.9%, 87.3%, 90.2%, 92.1% and 94.8% at the scan rates of 0.2, 0.4, 0.6, 0.8 and 1 mV·s⁻¹, respectively (Fig. 4(e)). From the CV curves of Fe_7S_8@NC-2 electrodes (Fig. 4(f)), the capacitive-controlled contribution dominates the overall charge storage process at 1.0 mV·s⁻¹, indicating the enhanced pseudocapacitance contribution with the increase of scan rates, which offers more excessive capacities at high current densities. The conspicuous pseudocapacitive contribution of Fe_7S_8@NC-2 can be attributed to the high specific surface area and N-doped carbon framework, which facilitate the surface charge storage. Above data meanwhile explain the origin of excess capacity of Fe_7S_8@NC-2 electrode.

Based on the above electrochemical results, the Fe_7S_8@NC-2 nanocomposite is the optimized electrode materials for LIBs. Besides, its sodium storage performance was tested. Figure 5(a) shows the CV curves for the initial three cycles at a scan rate of 0.1 mV·s⁻¹. In the first cathodic scan, a strong reduction peak at 0.7 V and a weak peak centered at 0.16 V is assigned as the formation of SEI film as well as the conversion reaction of Fe_7S_8 to form Fe and Na_2S [48]. During the subsequent two cycles, this peak at 0.7 V disappeared, and the broad cathodic peak at about 2.04 V is possibly corresponding to sodiation of Fe_7S_8 to Na_2FeS_2 [49], the wide peaks centered at 0.79 V and around 0.3 V are attributed to the main electrochemical reaction to form metallic Fe and Na_2S, respectively. The sharp
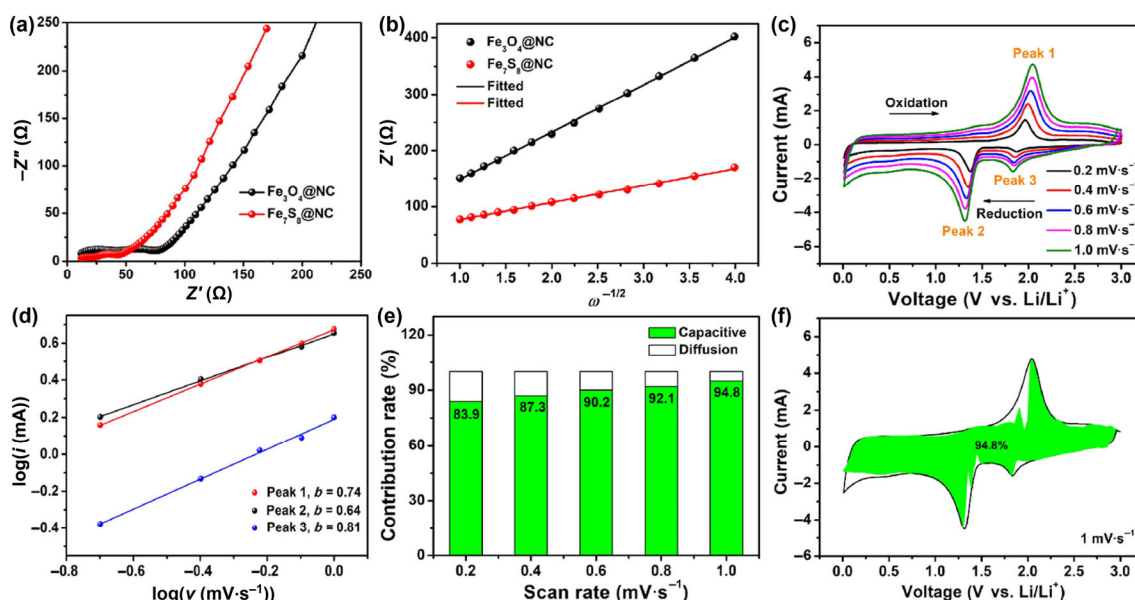

Figure 4 (a) Nyquist plots and (b) relationship between Z' and $\omega^{-1/2}$ in the low frequency region of cycled Fe_3O_4@NC and typical Fe_7S_8@NC electrodes. (c) CV curves at different scan rates. (d) Relationship between log i and log v of cathodic and anodic peaks. (e) Capacitive contribution rates. (f) CV curves with capacitive contribution to the charge storage at 1.0 mV·s⁻¹ of Fe_7S_8@NC-2 electrodes.
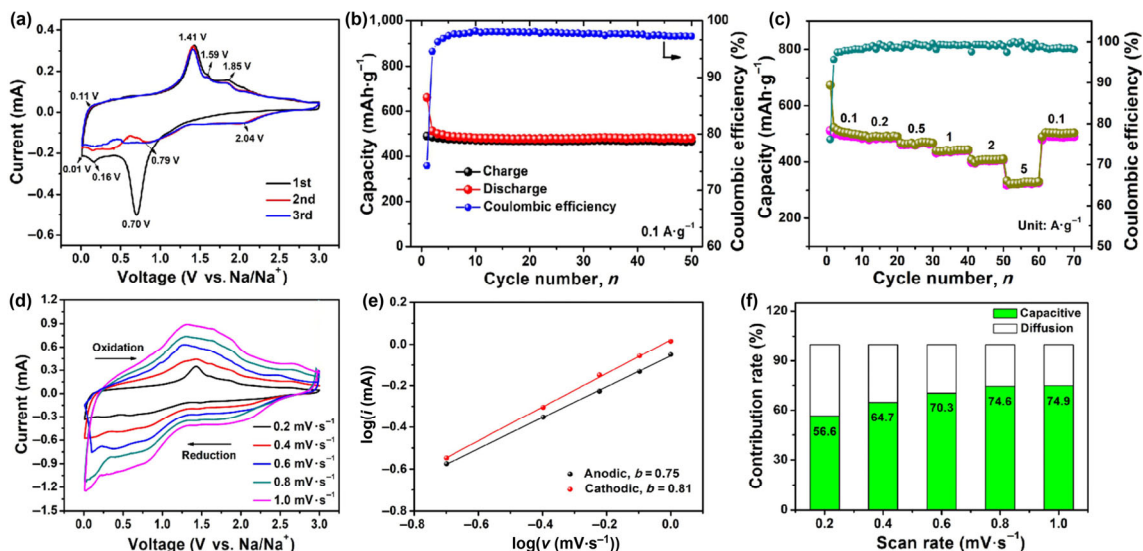
Figure 5 (a) CV curves for the first three cycles, (b) cycling performance at 0.1 A·g^{-1}, (c) rate capability at different current densities, (d) CV curves at different scan rates, (e) relationship between log i and log v of cathodic and anodic peaks, and (f) capacitive contribution rates of Fe$_7$S$_8$@NC-2 electrodes.

anodic peak at 1.41 V and weak peaks at 1.59 as well as 1.85 V correspond to the complicated multi-step oxidation of Fe metal to Na$_2$FeS$_2$, Na$_{2-x}$FeS$_2$ and Fe$_3$S$_4$ [50, 51]. The structure evolution process has been confirmed by *ex-situ* XRD and HRTEM techniques (Figs. S21 and S22 in the ESM). The overlap of CV curves after the first scan confirms the good reversibility of Fe$_7$S$_8$@NC nanocomposite. The galvanostatic discharge/charge profiles of Fe$_7$S$_8$@NC nanocomposite are in accordance with the CV curves (Fig. S23 in the ESM). The discharge and charge capacities for the first cycle are 703 and 526 mAh·g^{-1} with a CE of 74.8%. The initial irreversible capacity loss could be attributed to the formation of SEI layer on the surface of active materials and decomposition of electrolyte. Figure 5(b) shows its cycling performance at 0.1 A·g^{-1}, it exhibits a high reversible capacity of 468 mAh·g^{-1} over 50 cycles without any capacity loss. The related rate performance at various current densities is shown in Fig. 5(c). As observed, the Fe$_7$S$_8$@NC presents average capacities of 496, 485, 464, 437, 403 and 324 mAh·g^{-1} at current densities of 0.1, 0.2, 0.5, 1, 2 and 5 A·g^{-1}. When the current density reduces back to 0.1 A·g^{-1} after 70 cycles, the capacity can recover to 490 mAh·g^{-1}. Its high-rate cycling stability at 2 A·g^{-1} was further discussed (Fig. S24 in the ESM). The charge capacity can still maintain at 415 mAh·g^{-1} over 100 cycles, demonstrating good sodium storage performance, which is better than that of Fe$_7$S$_8$@C (Fig. S25 in the ESM) and comparable to the previous reports (Table S3 in the ESM). The TEM and SEM images of cycled Fe$_7$S$_8$@NC electrode show that the sphere-like morphology can be well-preserved, which demonstrates that the outer N-doped carbon layer can effectively buffer the volume changes of the electrode during the ion insertion/extraction process (Fig. S26 in the ESM).

The good sodium storage performance inspires us to study the electrochemical kinetics process of Fe$_7$S$_8$@NC-2 electrode. The small charge transfer impedance upon repeated cycles implies that a stable SEI film is formed on the surface of electrode, which contributes to the stable cycling performance (Fig. S27 and Table S4 in the ESM). GITT curves also give the similar conclusions (Fig. S28 in the ESM). The CV curves with various scan rates are shown in Fig. 5(d), the related oxidation and reduction peaks are not indistinctive with the increase of scan rate. The b value for oxidation and reduction peaks is calculated to be 0.75 and 0.81, respectively (Fig. 5(e)), indicating a mixture of diffusion-controlled and surface capacitance

contribution. Moreover, the capacitance contribution rates during overall charge storage process are shown in Fig. 5(f). The capacitance contribution rate gradually increases from 56.6% to 74.9% (from 0.2 to 1.0 mV·s^{-1}), implying the increased surface-controlled capacitance contribution. This can be attributed to the hierarchical Fe$_7$S$_8$ nano-aggregates, which provides more active sites for fast surface-controlled sodium storage.

DFT calculations were employed to verify the advantages of nitrogen doping into the Fe$_7$S$_8$@NC nanocomposite. The interactions between Fe$_7$S$_8$ and carbon with and without N-doping was studied. Figures 6(a)–6(d) show the optimized structures. The binding energies of original carbon layer, graphitic N pyridinic N and pyrrolic N with Fe$_7$S$_8$ are calculated to be −0.91, −1.49, −3.10, and −2.45 eV, respectively. It indicates that the N doping could overall enhance the binding ability of Fe$_7$S$_8$ on the carbon layer. Besides, the N doping carbon with rich electrons can increase the conductivity, benefiting for electron transfer during lithium or sodium storage process (Figs. 6(e)–6(h)). The two factors contribute to the better lithium or sodium storage performance compared with Fe$_7$S$_8$@C.

The excellent electrochemical performance of Fe$_7$S$_8$@NC motivates us to assemble the Li or Na-ion full cell (Figs. S29 and S30 in the ESM). The Fe$_7$S$_8$@NC//LiCoO$_2$ full cell shows good lithium storage performance (Fig. S29(c) in the ESM), the discharge capacity can maintain at 220 mAh·g^{-1} over 100 cycles. Figure S30(b) in the ESM shows the charge/discharge curves of Fe$_7$S$_8$@NC//Na$_3$V$_2$(PO$_4$)$_3$ full cell. Compared with that of LIBs, it presents an obvious voltage plateau and small electrode polarization. The cycling performance in Fig. S10(c) in the ESM shows that the discharge capacity approaches 200 mAh·g^{-1} after 100 cycles, demonstrating good cycling stability.

Based on the above electrochemical results, the excellent electrochemical performance of Fe$_7$S$_8$@NC nanocomposites is mainly attributed to the following factors: First, the Fe$_7$S$_8$ nano-aggregates could shorten the Li$^+$ or Na$^+$ diffusion path and enhance the Li$^+$ or Na$^+$ transport kinetics. Second, the void between Fe$_7$S$_8$ primary nanoparticles can provide some space to alleviate the volume changes of Fe$_7$S$_8$ upon repeated cycles. Third, the high conductivity of N-doped carbon layer can improve the electron transfer efficiency. Besides, the N atoms in the carbon framework can create more defects,
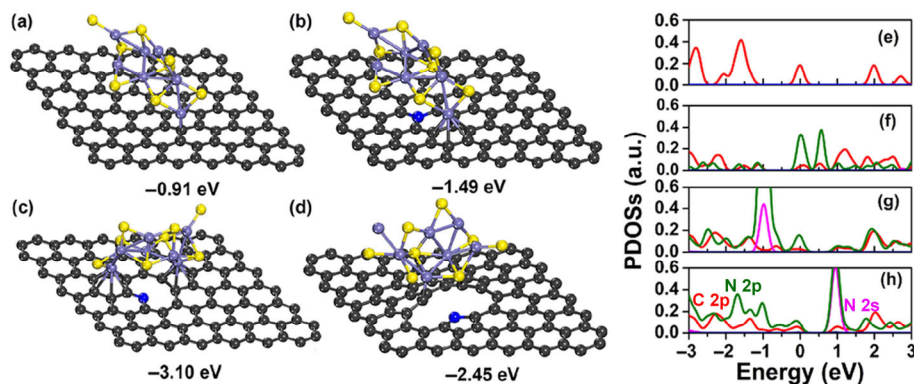
Figure 6 Schematic illustration of the Fe_7S_8 adsorbed onto perfect carbon layer (a), and that with graphitic N (b), pyridinic N (c), and pyrrolic N (d). Black, yellow, blue, purple represent C, S, N and Fe atoms, respectively. The adsorption energies are shown below the figures. Partial density of states (PDOSs) of carbon layer (e), and that with graphitic N (f), pyridinic N (g) and pyrrolic N (h), respectively. The Fermi level is set to 0.

which will offer numerous active sites to increase the lithium or sodium storage capacities. More importantly, the N-doped carbon layer as an effective protective layer can inhibit the particle pulverization of Fe_7S_8 induced by the big volume expansion, meanwhile suppress the dissolution of polysulfide into the electrolyte during the redox process. This study demonstrates that the N-doped carbon coated hierarchical Fe_7S_8 nanocomposites with appropriate carbon contents could serve as the potential anode materials for both LIBs and SIBs fields.

4   Conclusions

In summary, the core–shell structured Fe_7S_8@NC nanocomposites have been controllably prepared by a simple solution method and subsequent sulfuration process. As anode materials, these composites exhibit better cycling stability and rate capabilities than Fe_7S_8, Fe_3O_4@NC and Fe_7S_8@C. Among these electrodes, Fe_7S_8@NC nanocomposite obtained at 550 °C with a carbon layer thickness of 8 nm shows the highest capacity and best cycling stability for LIBs. The reversible capacity can maintain at 833 mAh·g^{-1} after 1,000 cycles at a high current density of 2 A·g^{-1}. Besides LIBs, the sodium storage performance of optimized Fe_7S_8@NC nanocomposite was tested. The electrochemical reaction kinetics results show that the combination of Fe_7S_8 nano-aggregates and N-doped carbon layer can improve the electron/ion transport kinetics and increase the surface-controlled capacitance contribution. The experimental and theoretical analyses show that the excellent lithium and sodium storage performances of Fe_7S_8@NC are mainly attributed to the well-designed core–shell hierarchical nanostructure of Fe_7S_8@NC and synergistic effect between Fe_7S_8 nano-aggregates and N-doped carbon layer. The above results imply that the Fe_7S_8@NC nanocomposites are promising anode materials for future energy storage fields.

Acknowledgements

Electronic Supplementary Material: Supplementary material (additional characterization results) is available in the online version of this article at https://doi.org/10.1007/s12274-020-2677-0

References

[1]   Armand, M.; Tarascon, J. M. Building better batteries. *Nature* **2008**, *451*, 652–657.

[2]   Ji, L. W.; Lin, Z.; Alcoutlabi, M.; Zhang, X. W. Recent developments in nanostructured anode materials for rechargeable lithium-ion batteries. *Energy Environ. Sci.* **2011**, *4*, 2682–2699.

[3]   Lu, C.; Li, Z. Z.; Xia, Z.; Ci, H. N.; Cai, J. S.; Song, Y. Z.; Yu, L. H.; Yin, W. J.; Dou, S. X.; Sun, J. Y. et al. Confining MOF-derived SnSe nanoplatelets in nitrogen-doped graphene cages via direct CVD for durable sodium ion storage. *Nano Res.* **2019**, *12*, 3051–3058.

[4]   Ohzuku, T.; Iwakoshi, Y.; Sawai, K. Formation of lithium-graphite intercalation compounds in nonaqueous electrolytes and their application as a negative electrode for a lithium ion (shuttlecock) cell. *J. Electrochem. Soc.* **1993**, *140*, 2490–2498.

[5]   Zhang, Z. J.; Zhao, H. L.; Du, Z. H.; Chang, X. W.; Zhao, L. N.; Du, X. F.; Li, Z. L.; Teng, Y. Q.; Fang, J. J.; Świerczek, K. (101) plane-oriented SnS_2 nanoplates with carbon coating: A high-rate and cycle-stable anode material for lithium ion batteries. *ACS Appl. Mater. Interfaces* **2017**, *9*, 35880–35887.

[6]   Zhou, Y. L.; Tian, J.; Xu, H. Y.; Yang, J.; Qian, Y. T. VS_4 nanoparticles rooted by a-C coated MWCNTs as an advanced anode material in lithium ion batteries. *Energy Storage Mater.* **2017**, *6*, 149–156.

[7]   Li, Z. Y.; Ottmann, A.; Zhang, T.; Sun, Q.; Meyer, H. P.; Vaynzof, Y.; Xiang J. H.; Klingeler, R. Preparation of hierarchical $C@MoS_2@C$ sandwiched hollow spheres for lithium ion batteries. *J. Mater. Chem. A* **2017**, *5*, 3987–3994.

[8]   Fang, Y.; Lv, Y. Y.; Gong, F.; Elzatahry, A. A.; Zheng, G. F.; Zhao, D. Y. Synthesis of 2D-mesoporous-carbon/MoS_2 heterostructures with well-defined interfaces for high-performance lithium-ion batteries. *Adv. Mater.* **2016**, *28*, 9385–9390.

[9]   Xie, J. J.; Liu, L.; Xia, J.; Zhang, Y.; Li, M.; Ouyang, Y.; Nie, S.; Wang, X. Y. Template-free synthesis of Sb_2S_3 hollow microspheres as anode materials for lithium-ion and sodium-ion batteries. *Nano-Micro Lett.* **2018**, *10*, 12.

[10] Jiang, F. Y.; Wang, Q.; Du, R.; Yan, X. S.; Zhou, Y. L. Fe_7S_8 nanoparticles attached carbon networks as anode materials for both lithium and sodium ion batteries. *Chem. Phys. Lett.* **2018**, *706*, 273–279.

[11] Choi, M. J.; Kim, J.; Yoo, J. K.; Yim, S.; Jeon, J.; Jung, Y. S. Extremely small pyrrhotite Fe_7S_8 nanocrystals with simultaneous carbon-encapsulation for high-performance Na–ion batteries. *Small* **2018**, *14*, 1702816.

[12] Chen, S. H.; Fan, L.; Xu, L. L.; Liu, Q.; Qin, Y.; Lu, B. G. 100 K cycles: Core-shell h-FeS@C based lithium-ion battery anode. *Energy Storage Mater.* **2017**, *8*, 20–27.

[13] Kumar, R.; Sahoo, S.; Joanni, E.; Singh, R. K.; Yadav, R. M.; Verma, R. K.; Singh, D. P.; Tan, W. K.; Del Pino, A. P.; Moshkalev, S. A. et al. A review on synthesis of graphene, h-BN and MoS_2 for energy

storage applications: Recent progress and perspectives. *Nano Res.* **2019**, *12*, 2655–2694.

[14] Fan, H. H.; Li, H. H.; Guo, J. Z.; Zheng, Y. P.; Huang, K. C.; Fan, C. Y.; Sun, H. Z.; Li, X. F.; Wu, X. L.; Zhang, J. P. Target construction of ultrathin graphitic carbon encapsulated FeS hierarchical microspheres featuring superior low-temperature lithium/sodium storage properties. *J. Mater. Chem. A* **2018**, *6*, 7997–8005.

[15] Zhu, J. H.; Chen, Z.; Jia, L.; Lu, Y. Q.; Wei, X. Q.; Wang, X. N.; Wu, W. N.; Han, N.; Li, Y. G.; Wu, Z. X. Solvent-free nanocasting toward universal synthesis of ordered mesoporous transition metal sulfide@N-doped carbon composites for electrochemical applications. *Nano Res.* **2019**, *12*, 2250–2258.

[16] Xu, Y. X.; Li, W. Y.; Zhang, F.; Zhang, X. L.; Zhang, W. J.; Lee, C. S.; Tang, Y. B. *In situ* incorporation of FeS nanoparticles/carbon nanosheets composite with an interconnected porous structure as a high-performance anode for lithium ion batteries. *J. Mater. Chem. A* **2016**, *4*, 3697–3703. `

[17] Liu, J.; Wen, Y.; R.; Wang, Y.; Van Aken, P. A.; Maier, J.; Yu, Y. Carbon-encapsulated pyrite as stable and earth-abundant high energy cathode material for rechargeable lithium batteries. *Adv. Mater.* **2014**, *26*, 6025–6030.

[18] Zhang, D.; Mai, Y. J.; Xiang, J. Y.; Xia, X. H.; Qiao, Y. Q.; Tu, J. P. FeS$_2$/C composite as an anode for lithium ion batteries with enhanced reversible capacity. *J. Power Sources* **2012**, *217*, 229–235.

[19] Hou, T. Z.; Chen, X.; Peng, H. J.; Huang, J. Q.; Li, B. Q.; Zhang, Q.; Li, B. Design principles for heteroatom-doped nanocarbon to achieve strong anchoring of polysulfides for lithium-sulfur batteries. *Small* **2016**, *12*, 3283–3291.

[20] Xiao, S.; Liu, S. H.; Zhang, J. Q.; Wang, Y. Polyurethane-derived N-doped porous carbon with interconnected sheet-like structure as polysulfide reservoir for lithium-sulfur batteries. *J. Power Sources* **2015**, *293*, 119–126.

[21] Zhong, Y. T.; Li, B.; Li, S. M.; Xu, S. Y.; Pan, Z. H.; Huang, Q. M.; Xing, L. D.; Wang, C. S.; Li, W. S. Bi nanoparticles anchored in N-doped porous carbon as anode of high energy density lithium ion battery. *Nano-Micro Lett.* **2018**, *10*, 56.

[22] Lu, C.; Li, Z. Z.; Yu, L. H.; Zhang, L.; Xia, Z.; Jiang, T.; Yin, W. J.; Dou, S. X.; Liu, Z. F.; Sun, J. Y. Nanostructured Bi$_2$S$_3$ encapsulated within three-dimensional N-doped graphene as active and flexible anodes for sodium-ion batteries. *Nano Res.* **2018**, *11*, 4614–4626.

[23] Jiang, F. Y.; Liu, Y. Z.; Wang, Q.; Zhou, Y. L. Hierarchical Fe$_3$O$_4$@NC composites: Ultra-long cycle life anode materials for lithium ion batteries. *J. Mater. Sci.* **2018**, *53*, 2127–2136.

[24] Wei, X. J.; Tan, X.; Meng, J. S.; Wang, X. P.; Hu, P.; Yang, W.; Tan, S. S.; An, Q. Y.; Mai, L. Q. Amine-assisted synthesis of FeS@N-C porous nanowires for highly reversible lithium storage. *Nano Res.* **2018**, *11*, 6206–6216.

[25] Liu, Y. Z.; Zhong, W. T.; Yang, C. G.; Pan, Q. Z.; Li, Y. P.; Wang, G.; Zheng, F. H.; Xiong, X. H.; Liu, M. L.; Zhang, Q. Y. Direct synthesis of FeS/N-doped carbon composite for high-performance sodium-ion batteries. *J. Mater. Chem. A* **2018**, *6*, 24702–24708.

[26] Xiao, Y.; Wang, X.; Wang, W.; Zhao, D.; Cao, M. H. Engineering hybrid between MnO and N-doped carbon to achieve exceptionally high capacity for lithium-ion battery anode. *ACS Appl. Mater. Interfaces* **2014**, *6*, 2051–2058.

[27] Veerasubramani, G. K.; Subramanian, Y.; Park, M. S.; Nagaraju, G.; Senthilkumar, B.; Lee, Y. S.; Kim, D. W. Enhanced storage ability by using a porous pyrrhotite@N-doped carbon yolk-shell structure as an advanced anode material for sodium-ion batteries. *J. Mater. Chem. A* **2018**, *6*, 20056–20068.

[28] Yuan, J.; Hu, X.; Chen, J. X.; Liu, Y. J.; Huang, T. Z; Wen, Z. H. *In situ* formation of vanadium nitride quantum dots on N-doped carbon hollow spheres for superior lithium and sodium storage. *J. Mater. Chem. A* **2019**, *7*, 9289–9296.

[29] Zhou, Y. L.; Li, Y. Y.; Wang, Q. Q.; Du, R.; Zhang, M.; Sun, X. Q.; Zhang, X. Y.; Kang, L. T; Jiang, F. Y. Ultrasmall MoS$_3$ loaded GO nanocomposites as high-rate and long-cycle-life Anode Materials for lithium- and sodium-ion batteries. *ChemElectroChem* **2019**, *6*, 3113–3119.

[30] Long, B.; Zhang, J. N.; Luo, L.; Ouyang, G. F.; Balogun, M. S.; Song, S. Q; Tong, Y. X. High pseudocapacitance boosts the performance of monolithic porous carbon cloth/closely packed TiO$_2$ nanodots as an anode of an all-flexible sodium-ion battery. *J. Mater. Chem. A* **2019**, *7*, 2626–2635.

[31] Hansson, E. B.; Odziemkowski, M. S.; Gillham, R. W. Formation of poorly crystalline iron monosulfides: Surface redox reactions on high purity iron, spectroelectrochemical studies. *Corr. Sci.* **2006**, *48*, 3767–3783.

[32] Bulusheva, L. G.; Okotrub, A. V.; Fedoseeva, Y. V.; Kurenya, A. G.; Asanov, I. P.; Vilkov, O. Y.; Koós, A. A.; Grobert, N. Controlling pyridinic, pyrrolic, graphitic, and molecular nitrogen in multi-wall carbon nanotubes using precursors with different N/C ratios in aerosol assisted chemical vapor deposition. *Phys. Chem. Chem. Phys.* **2015**, *17*, 23741–23747.

[33] Zhang, K. L.; Zhang, T. W.; Liang, J. W.; Zhu, Y. C.; Lin, N.; Qian, Y. T. A potential pyrrhotite (Fe$_7$S$_8$) anode material for lithium storage. *RSC Adv.* **2015**, *5*, 14828–14831.

[34] Guo, Y. M.; Zhang, L. J.; Wang, J. T.; Liang, J. M.; Xi, L. D. G. Facile method for adjustable preparation of nano-Fe$_7$S$_8$ supported by carbon as the anode for enhanced lithium/sodium storage properties in Li/Na-ion batteries. *Electrochim. Acta* **2019**, *322*, 134763.

[35] Liu, M. T.; Deng, X.; Ma, Y. D.; Xie, W. H.; Hou, X. Y.; Fu, Y. J.; He, D. Y. Well-designed hierarchical Co$_3$O$_4$ architecture as a long-life and ultrahigh rate capacity anode for advanced lithium-ion batteries. *Adv. Mater. Interfaces* **2017**, *4*, 1700553.

[36] Zhou, Y. L.; Yan, D.; Xu, H. Y.; Feng, J. K.; Jiang, X. L.; Yue, J.; Yang, J.; Qian, Y. T. Hollow nanospheres of mesoporous Co$_9$S$_8$ as a high-capacity and long-life anode for advanced lithium ion batteries. *Nano Energy* **2015**, *12*, 528–537.

[37] Li, L. S.; Cabán-Acevedo, M.; Girard, S. N.; Jin, S. High-purity iron pyrite (FeS$_2$) nanowires as high-capacity nanostructured cathodes for lithium-ion batteries. *Nanoscale* **2014**, *6*, 2112–2118.

[38] Reddy, M.; Yu, T.; Sow, C. H.; Shen, Z. X.; Lim, C. T.; Subba Rao, G. V.; Chowdari, B. V. R. α-Fe$_2$O$_3$ nanoflakes as an anode material for li-ion batteries. *Adv. Funct. Mater.* **2007**, *17*, 2792–2799.

[39] Zhang, D. W.; Chen, C. H.; Zhang, J.; Ren, F. Novel electrochemical milling method to fabricate copper nanoparticles and nanofibers. *Chem. Mater.* **2005**, *17*, 5242–5245.

[40] Wang, X. Y.; Hao, H.; Liu, J. L.; Huang, T.; Yu, A. S. A novel method for preparation of macroposous lithium nickel manganese oxygen as cathode material for lithium ion batteries. *Electrochim. Acta* **2011**, *56*, 4065–4069.

[41] Hu, X.; Liu, Y. J.; Chen, J. X.; Jia, J. C.; Zhan, H. B.; Wen, Z. H. FeS quantum dots embedded in 3D ordered macroporous carbon nanocomposite for high-performance sodium-ion hybrid capacitors. *J. Mater. Chem. A* **2019**, *7*, 1138–1148.

[42] Lindström, H.; Södergren, S.; Solbrand, A.; Rensmo, H.; Hjelm, J.; Hagfeldt, A.; Lindquist, S. E. Li$^+$ ion insertion in TiO$_2$ (anatase). 2. Voltammetry on nanoporous films. *J. Phys. Chem. B* **1997**, *101*, 7717–7722.

[43] Fang, G. Z.; Wu, Z. X.; Zhou, J.; Zhu, C. Y.; Cao, X. X.; Lin, T. Q.; Chen, Y. M.; Wang, C.; Pan, A. Q.; Liang, S. Q. Observation of pseudocapacitive effect and fast ion diffusion in bimetallic sulfides as an advanced sodium‐ion battery anode. *Adv. Energy Mater.* **2018**, *8*, 1703155.

[44] Hong, Z. S.; Zhen, Y. C.; Ruan, Y. R.; Kang, M. L.; Zhou, K. Q.; Zhang, J. M.; Huang, Z. G.; Wei, M. D. Rational design and general synthesis of S-doped hard carbon with tunable doping sites toward excellent Na-ion storage performance. *Adv. Mater.* **2018**, *30*, 1802035.

[45] Wang, J.; Polleux, J.; Lim, J.; Dunn, B. Pseudocapacitive contributions to electrochemical energy storage in TiO$_2$ (anatase) nanoparticles. *J. Phys. Chem. C* **2007**, *111*, 14925–14931.

[46] Zhou, L. M.; Zhang, K.; Sheng, J. Z.; An, Q. Y.; Tao, Z. L.; Kang, Y. M.; Chen, J.; Mai, L. Q. Structural and chemical synergistic effect of CoS nanoparticles and porous carbon nanorods for high-performance sodium storage. *Nano Energy* **2017**, *35*, 281–289.

[47] Hou, B. H.; Wang, Y. Y.; Guo, J. Z.; Ning, Q. L.; Xi, X, T.; Pang, W. L.; Cao, A. M.; Wang, X. L.; Zhang, J. P.; Wu, X. L. Pseudocapacitance-boosted ultrafast Na storage in a pie-like FeS@C nanohybrid as an advanced anode material for sodium-ion full batteries. *Nanoscale* **2018**, *10*, 9218–9225.

[48] Jin, A. H.; Kim, M. J.; Lee, K. S.; Yu, S. H.; Sung, Y. E. Spindle-like Fe$_7$S$_8$/N-doped carbon nanohybrids for high-performance sodium ion battery anodes. *Nano Res*. **2019**, *12*, 695–700.

[49] Huang, W.; Sun, H. Y.; Shangguan, H. H.; Cao, X. Y.; Xiao, X. Y.; Shen, F.; Mølhave, K.; Ci, L. J.; Si, P. C.; Zhang, J. D. Three-dimensional iron sulfide-carbon interlocked graphene composites for high-performance sodium-ion storage. *Nanoscale* **2018**, *10*, 7851–7859.

[50] Zhang, C. Z.; Han, F.; Ma, J. M.; Li, Z.; Zhang, F. Q.; Xu, S. H.; Liu, H. B.; Li, X. K.; Liu, J. S.; Lu, A. H. Fabrication of strong internal electric field ZnS/Fe$_9$S$_{10}$ heterostructures for highly efficient sodium ion storage. *J. Mater. Chem. A* **2019**, *7*, 11771–1178.

[51] Chen, W. H.; Zhang, X. X.; Mi, L. W.; Liu, C. T.; Zhang, J. M.; Cui, S. Z.; Feng, X. M.; Cao, Y. L.; Shen, C. Y. High-performance flexible freestanding anode with hierarchical 3D carbon-networks/Fe$_7$S$_8$/graphene for applicable sodium-ion batteries. *Adv. Mater.* **2019**, *30*, 1806664.